1-1-2019

Identification of active sites for acidic oxygen reduction on carbon catalysts with and without nitrogen doping

Yi Jia
Griffith University

Longzhou Zhang
Griffith University, Yunnan University

Linzhou Zhuang
University of Queensland

Hongli Liu
Qingdao University

Xuecheng Yan
Griffith University

See next page for additional authors

Identification of active sites for acidic oxygen reduction on carbon catalysts with and without nitrogen doping

Abstract

Owing to the difficulty in controlling the dopant or defect types and their homogeneity in carbon materials, it is still a controversial issue to identify the active sites of carbon-based metal-free catalysts. Here we report a proof-of-concept study on the active-site evaluation for a highly oriented pyrolytic graphite catalyst with specific pentagon carbon defective patterns (D-HOPG). It is demonstrated that specific carbon defect types (an edged pentagon in this work) could be selectively created via controllable nitrogen doping. Work-function analyses coupled with macro and micro-electrochemical performance measurements suggest that the pentagon defects in D-HOPG served as major active sites for the acidic oxygen reduction reaction, even much superior to the pyridinic nitrogen sites in nitrogen-doped highly oriented pyrolytic graphite. This work enables us to elucidate the relative importance of the specific carbon defects versus nitrogen-dopant species and their respective contributions to the observed overall acidic oxygen reduction reaction activity.

Disciplines

Engineering | Physical Sciences and Mathematics

Publication Details

Jia, Y., Zhang, L., Zhuang, L., Liu, H., Yan, X., Wang, X., Liu, J., Wang, J., Zheng, Y., Xiao, Z., Taran, E., Chen, J., Yang, D., Zhu, Z., Wang, S., Dai, L. & Yao, X. (2019). Identification of active sites for acidic oxygen reduction on carbon catalysts with and without nitrogen doping. Nature Catalysis, 2 688-695.

Authors

Yi Jia, Longzhou Zhang, Linzhou Zhuang, Hongli Liu, Xuecheng Yan, Xin Wang, Jiandang Liu, Jiancheng Wang, Yarong Zheng, Zhaohui Xiao, Elena Taran, Jun Chen, Dongjiang Yang, Zhonghua Zhu, Shuangyin Wang, Liming Dai, and Xiangdong Yao

Identification of active sites for acidic oxygen reduction on carbon catalysts with and without nitrogen-doping

Yi Jia,[1⊥] Longzhou Zhang,[1,2⊥] Linzhou Zhuang,[3] Hongli Liu,[4] Xuecheng Yan,[1] Xin Wang,[1,5] Jiandang Liu,[5] Jiancheng Wang,[6] Yarong Zheng,[5] Zhaohui Xiao,[7] Elena Taran,[8] Jun Chen,[9] Dongjiang Yang,[4] Zhonghua Zhu,[3] Shuangyin Wang,[7] Liming Dai[10*] and Xiangdong Yao[1,11*]

[1]School of Environment and Science, Queensland Micro- and Nanotechnology Centre, Griffith University, Nathan Campus, Queensland 4111, Australia.

[2]School of Materials Science and Engineering, Yunnan Key Laboratory for Micro/nano Materials & Technology, Yunnan University, Kunming, Yunnan 650091, P. R. China.

[3]School of Chemical Engineering, the University of Queensland, Queensland 4072, Australia.

[4]Collaborative Innovation Center for Marine Biomass Fibers, Materials and Textiles of Shandong Province, Institute of Marine Biobased Materials, College of Environmental Science and Engineering, Qingdao University, Qingdao 266071, P. R. China.

[5] Division of Nanomaterials and Chemistry, Hefei National Laboratory for Physical Sciences at the Microscale, Collaborative Innovation Center of Suzhou Nano Science and Technology, Department of Chemistry, University of Science and Technology of China, Hefei, P. R. China.

[6]Key Laboratory of Coal Science and Technology, Taiyuan University of Technology, Ministry of Education and Shanxi Province, Taiyuan 030024, P. R. China.

[7]State Key Laboratory of Chem/Bio-Sensing and Chemometrics, College of Chemistry and Chemical Engineering, Hunan University, Changsha 410082, P. R. China.

[8]Australian Institute for Bioengineering and Nanotechnology, The University of Queensland, Australian National Fabrication Facility-Queensland Node, St. Lucia, Queensland 4072, Australia.

[9]Intelligent Polymer Research Institute, ARC Centre of Excellence for Electromaterials Science, AIIM Facility, University of Wollongong, Innovation Campus, Wollongong, New South Wales 2522, Australia.

[10] CWRU-UNSW International Joint Laboratory, Department of Macromolecular Science and Engineering, Case Western Reserve University, 10900 Euclid Avenue, Cleveland, OH 44106, USA.

[11]State Key Laboratory of Inorganic Synthesis and Preparative Chemistry, College of Chemistry, Jilin University, Changchun 130012, P. R. China.

[⊥]Y. Jia and L. Z. Zhang contributed equally.

E-mail: liming.dai@case.edu and x.yao@griffith.edu.au

Abstract

Owing to the difficulty in controlling the dopant or defect types and their homogeneity in carbon materials, it is still a controversial issue to identify the active sites of carbon-based metal-free catalysts. Herein, we report a proof of concept study on the active-site evaluation for a highly oriented pyrolytic graphite catalyst with specific pentagon carbon defective patterns (D-HOPG). It is demonstrated that specific carbon defect types (edged pentagon in this work) could be selectively created *via* controllable N-doping. Work function analyses coupled with macro/micro-electrochemical performance measurements suggest that the pentagon defects in D-HOPG served as major active sites for acidic oxygen reduction reaction (ORR), even much superior to the pyridinic nitrogen sites in N-doped highly oriented pyrolytic graphite (N-HOPG). This work enables us to elucidate the relative importance of the specific carbon defects *vs* N-dopant species and their respective contributions to the observed overall acidic ORR activity.

Carbon-based metal-free catalysts (CMFCs) have been widely exploited as the potential alternatives to the expensive Pt catalysts for oxygen reduction reaction (ORR) since the nitrogen-doped carbon nanotubes was reported to be active for ORR in 2009[1]. Although tremendous progress on the development of new doping strategies[2-10] for CMFCs has been made so far, the detailed catalytic mechanism and the identification of active sites (i.e. specific doping sites in sp^2 carbon topological structures) still remains controversial. For N-doped CMFCs, for instance, some reports have suggested that the pyridinic N (the nitrogen substituting a sp^2 carbon atom in a pyridinic ring on the edge) is responsible for the ORR catalytical activity[9,11,12] whereas other studies have indicated that the active sites are associated with the graphitic N (the nitrogen substituting a sp^2 carbon atom in the plane and bonding to three carbon atoms)[13-15]. Of particular interest, Guo *et al.*[16] deliberately designed an experiment in 2016, for the first time, to control the type of pyridinic N (Pr-N) or graphitic N (G-N) species up to an extremely high percentage (>90%). Furthermore, the G-N was characterized to be ORR inactive while the Pr-N exhibited acidic ORR activity. Consequently, these authors concluded that the Pr-N, but not the G-N, is the active site for acidic ORR[16]. However, further confirmation is required to support the above conclusion due to the following several critical issues: i) Certain topological defects have been recently demonstrated to be highly active for ORR even with a much superior ORR activity to the N-doped counterparts[17-23]; ii) the N-doped sites have been reported to be inactive for ORR in acidic media due to protonation of the Pr-N to reduce the O_2 affinity[24]; and iii) it is virtually impossible to completely eliminate topological vacancy defects in the N-doped carbons. Therefore, it is important to identify the real active site for acidic ORR: vacancy-type defect or N-dopant? For this purpose, controlled synthesis of carbon defects (e.g. defect type, density and location) is urgently

needed, but rarely reported, to establish the correlation between the carbon defects and ORR performance[23,25].

To address the aforementioned critical points, we performed a proof of concept study. Specifically, we firstly synthesized the Pr-N dominated highly oriented pyrolytic graphite (N-HOPG) with an N content from 0.74~2.73 at% by following the same procedures of Guo *et al*[16]. Our combined Raman and positron annihilation (PA) measurements demonstrate that the removal of the Pr-N in N-HOPG can lead to the controllable formation of the edged pentagon carbon defects in the resultant defective HOPG (D-HOPG). Remarkably, subsequent micro-electrochemical measurements, coupled with work function analyses, reveal that the D-HOPG thus prepared show a significantly enhanced acidic ORR activity that is directly proportional to the number of defects, and that such defect-based active sites are mainly located at the edges of groove structures in the D-HOPG. Density functional theory (DFT) calculations indicate that the apexes of the edged pentagon defects are the preferential active sites for ORR with the highest onset potential of 0.74 eV. In this study, the formation mechanism of this edged pentagon defect is also investigated, both experimentally and theoretically, and our work represents a breakthrough in the development of high-performance metal-free catalysts for acidic ORR by controllable synthesis of desirable defects.

Results

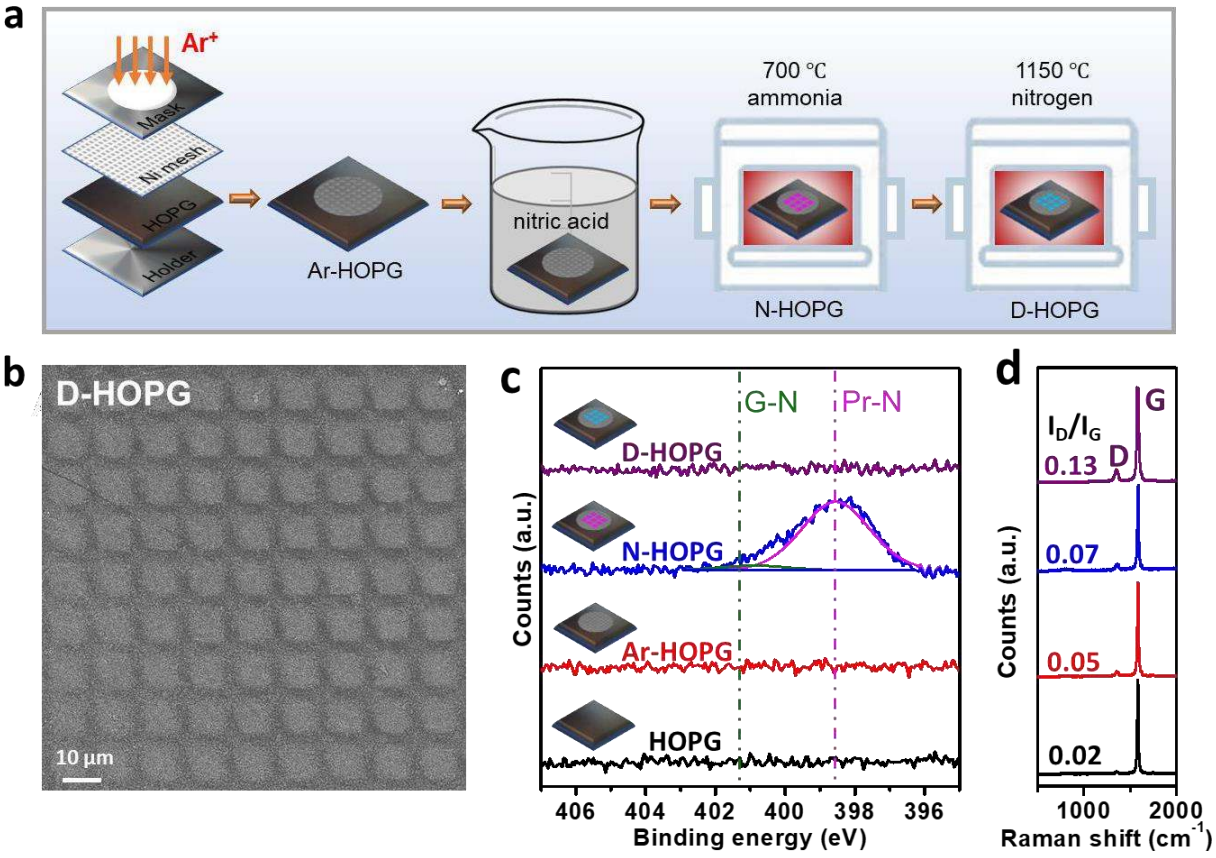

Fig. 1 | Synthetic scheme and structure characterization of D-HOPG. a, Synthetic scheme for the preparation of D-HOPG sample. **b,** SEM image of D-HOPG. **c,** The N 1s high resolution XPS spectra of HOPG, Ar-HOPG, N-HOPG and D-HOPG. **d,** The Raman spectra of HOPG, Ar-HOPG, N-HOPG and D-HOPG.

Synthetic strategy of specific carbon defect. Fig. 1a shows the synthetic procedure of D-HOPG using a well-controlled patterning method. Briefly, the pristine HOPG with a perfect graphitic carbon structure was etched by argon plasma to form uniform grooves through a nickel mesh with square windows (Supplementary Fig. 1). Then, the obtained sample (Ar-HOPG) was washed with nitric acid for three times to remove the residual nickel on the surface, followed by annealing at 700 °C for 3 hours in the ammonia flow. Consequently, this allows the specific N-dopant (Pr-N)

formed at the edge of N-HOPG grooves. Finally, the N-HOPG was further annealed at 1150 °C for 2 hours under nitrogen to obtain D-HOPG. Scanning electron microscopy (SEM) and atomic force microscopy (AFM) images (Fig. 1b and Supplementary Fig. 2) show that the ordered uniform square groove structures (length and depth sizes of ~10 μm and 160 nm, respectively) are uniformly distributed over the surface of D-HOPG. Such abundant groove structures provide sufficient docking sites for doping nitrogen atoms at the edge region of the carbon matrix. The X-ray photoelectron spectroscopy (XPS) spectra (Fig. 1c) indicate that the nitrogen doped N-HOPG is dominated by the pyridinic nitrogen (398.7 eV) with trace graphitic nitrogen (401.3 eV), well consistent to the study by Guo *et al*[16]. To eliminate the nitrogen dopants, we use the same nitrogen removal method as reported in our previous publication[23]. The XPS results (Fig. 1c) reveal that the nitrogen dopant is absent from the resultant D-HOPG. The corresponding Raman spectra (Fig. 1d) show an increased disorder level (the ratio of I_D/I_G) according to the order of HOPG < Ar- HOPG < N-HOPG < D-HOPG. The increased number of defects from N-HOPG to D-HOPG clearly indicates that new defects are generated due to the removal of nitrogen dopants. The X-ray absorption near edge structure (XANES) curves of N-HOPG and D-HOPG (Supplementary Fig. 3) show sharp peaks around 285.2 eV, contributed by the transition of the C 1s core electron to the π* state[26]. The intensity of the π* state of D-HOPG is weaker than that of N-HOPG, revealing the disruption of sp^2-hybridized carbon structure in the process of nitrogen removal associated with the reconstruction of the fragmentary carbon lattice.

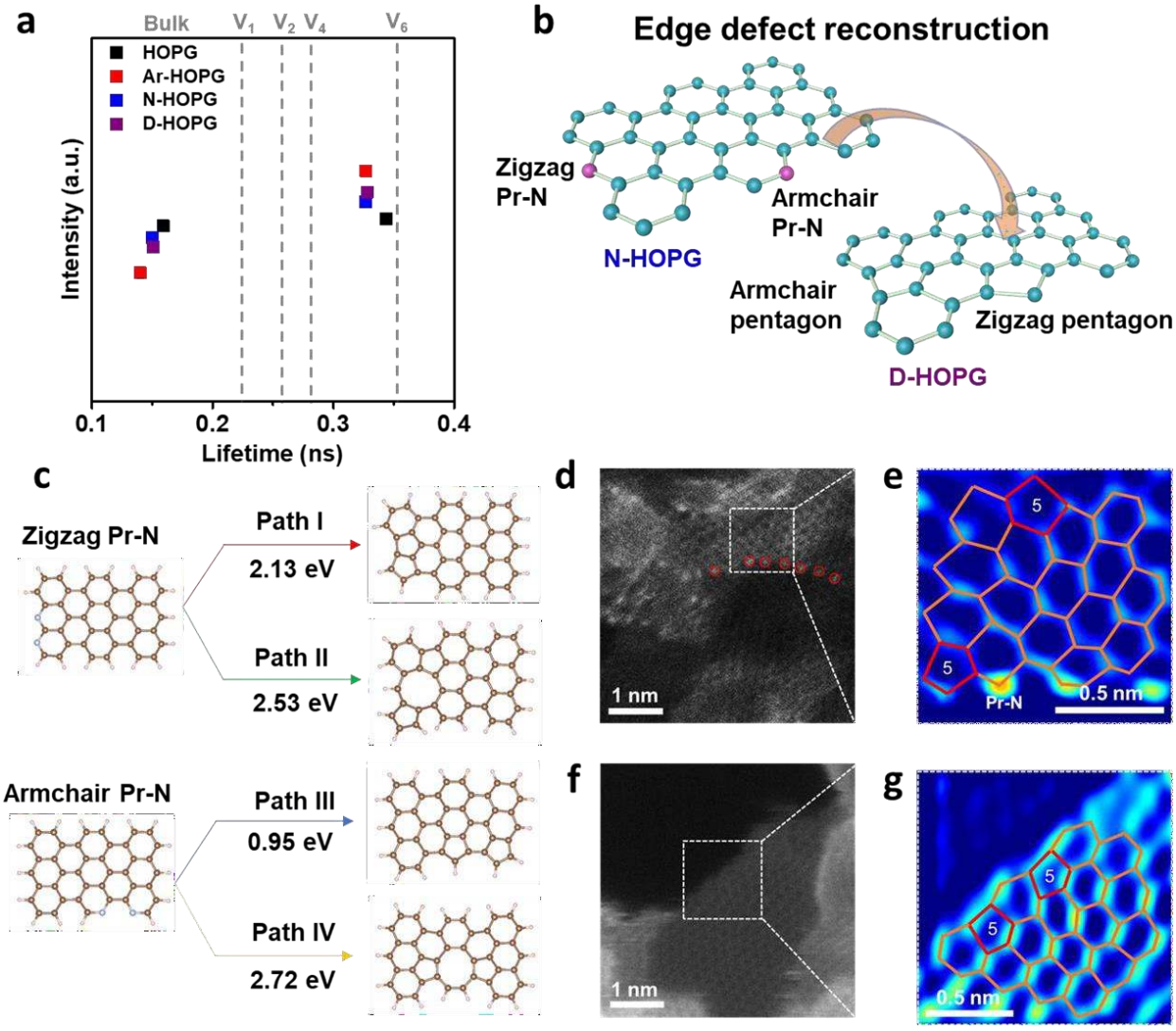

Fig. 2 | Structure characterization on formation of specific carbon defect via controllable N-doping species. a, Positron annihilation intensities versus the lifetimes for the samples of HOPG, Ar-HOPG, N-HOPG and D-HOPG. **b,** Illustration of edge defect reconstruction originated from nitrogen removal. **c,** Four reaction pathways of forming specific carbon defects derived from zigzag and armchair Pr-N models, respectively. **d,** The HAADF-STEM image of N-doped graphene (denoted as N-G). The nitrogen atoms are marked with red circles. **e,** The partially zoomed-in image of N-G. The grey scale is transformed to colour gradient. **f,** The HAADF-STEM image of derived defective graphene

(denoted as D-G). **g,** The partially zoomed-in image of D-G. The grey scale is transformed to colour gradient.

Positron annihilation (PA) was conducted to further investigate the types of defects in HOPG samples (Fig. 2a and Supplementary Table 1). The theoretical lifetimes of PA in different vacancy type defects (V_1 denotes single vacancy, etc.) are marked as the grey dashed lines in Fig. 2a. Two identical lifetimes (0.15 and 0. 34 ns) with similar signal intensities of PA are obtained in D-HOPG and N-HOPG, respectively, indicating the equivalent densities of intrinsic carbon lattice defects and V_x defects (x=5 or 6 denotes the absent numbers of carbon atoms in vacancy). Therefore, these results confirm that the increased overall defect numbers in D-HOPG (indicated by the higher I_D/I_G) should be attributed to the reconstruction of edge carbon lattice from N-HOPG (e.g., transformation of the pyridinic nitrogen ring into a pentagon) rather than the pre-existed vacancy defects. Fig. 2b illustrates the evolution of structure reconstruction from the zigzag and armchair Pr-N doped edge carbon lattice to the corresponding pentagon edge carbon defects.

While the removal of one Pr-N atom will result in the formation of one pentagon on the edge, two adjacent single vacancies on graphene are easy to coalesce and transform into a di-vacancy[18]. However, it is still uncertain whether two pentagons or a di-vacancy will be formed if two adjacent Pr-N atoms are removed. To investigate the defect type after the nitrogen removal, the formation energies of different model structures after removing two adjacent Pr-N are calculated, as shown in Fig. 2c. It can be seen that no matter for the armchair or the zigzag edge, the formation energies of two pentagons are smaller than that of a di-vacancy, implying that the defect type on the edges of D-HOPG is most likely the reconstructed pentagon carbon defect. To directly identify the formation of specific carbon defect *via* controllable N-doping species, we have carried out the high-angle annular dark-field scanning transmission electron microscopy (HAADF-STEM) on the

nitrogen-doped graphene (N-G) and defective graphene (D-G) with a probe-corrected TEM to simulate the defect formation on D-HOPG (i.e. N-G and D-G are synthesized by the identical N-doping-removal method on HOPG). Fig. 2d shows the HAADF-STEM image of N-G, in which the bright spots attributable to nitrogen atoms are observed to dominantly distribute on the edges of the graphene sheet. It is further observed that the N-dopants at the edge sites are in the form of Pr-N (Fig. 2e). After the high temperature treatment to remove the N atoms, the bright spots become invisible on the D-G image (Fig. 2f), suggesting that the N dopants are removed from the graphene sheet. Due to the disruption of the hexagonal topological structure of the carbon matrix caused by nitrogen elimination, the dangling bonds of carbon atoms are reunited to generate the non-hexagonal carbon lattice structures (i.e. carbon defects) (Fig. 2g), as indicated by the theoretical prediction (Fig. 2c). Clearly, therefore, the carbon defect type can be experimentally controlled by removing specific N doping site(s).

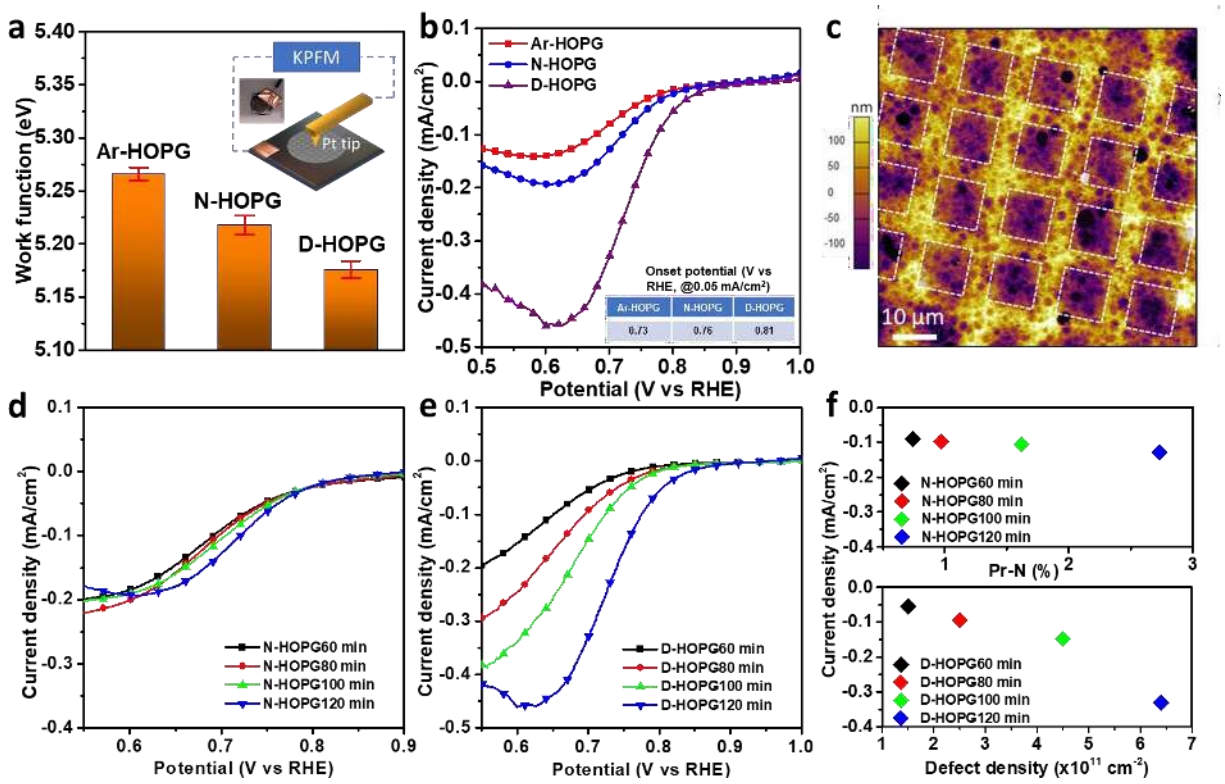

Fig. 3 | The intrinsic work function analysis and macro-electrocatalytic effects of N dopant and carbon defect in acidic ORR. a, The local work functions collected from the edge areas of Ar-HOPG, N-HOPG and D-HOPG. The Scheme of Kelvin probe force microscope (KPFM) test is shown as the inset. Error bars correspond to s.d. from three independent measurements. **b,** The LSV curves of Ar-HOPG, N-HOPG and D-HOPG for ORR in 0.1 M H_2SO_4 solution. The correlated onset potentials are shown in the inset table. **c,** The AFM image of D-HOPG after acidic ORR measurement. **d,** ORR activities of N-HOPG with the etching time from 60 min to 120 min. **e**, ORR activities of D-HOPG with the etching time from 60 min to 120 min. **f**, Correlation comparison between current densities of ORR at 0.7 V vs RHE (fastest kinetics variation of ORR) and pyridinic N concentrations/defect densities.

Work function analysis and electrochemical performance. Theoretically, the electron donating capability of a catalyst determines the interfacial charge transfer with the associated oxygen, having profound significance to ORR. To distinguish the ORR activity of the pyridinic nitrogen from that of the topological carbon defect, we use the local work functions obtained from Kelvin probe force microscope (KPFM) measurements[27] to evaluate the electron donating capability of N-HOPG and D-HOPG. Fig. 3a represents the local work functions of Ar-HOPG, N-HOPG and D-HOPG collected from each edge area using a Pt tip as the cantilever (the scheme is the inset in Fig. 3a). As can be seen, D-HOPG possesses the lowest local work function at the edge area (5.18 eV) while N-HOPG and Ar-HOPG have a higher local work functions of 5.22 eV and 5.27 eV, respectively, indicating the highest electron-donating capability for the defect generated by nitrogen removal. As expected, the corresponding linear scan voltammogram (LSV) curves in Fig. 3b show an efficient ORR activity for D-HOPG with an onset potential of 0.81 V vs RHE at 0.05 mA/cm^2 in an oxygen saturated 0.1 M H_2SO_4 aqueous solution at room temperature in a three-electrode system. Meanwhile, the onset potentials of Ar-HOPG and N-HOPG are 0.73 and 0.76 V vs RHE, respectively, both inferior to that of D-HOPG (Fig. 3b inset). Fig. 3c shows that the ordered square groove structures in D-HOPG are retained after the acidic ORR measurements.

To more quantitatively interpret the origin of ORR activities from N-HOPG and D-HOPG, we evaluated the electrocatalytic performance of various N-HOPG and D-HOPG samples treated by plasma etching for different times. Fig. 3d shows the LSV curves for the N-HOPG 60 min (0.74% N), N-HOPG 80 min (0.97% N), N-HOPG 100 min (1.62% N), and N-HOPG 120 min (2.73% N), respectively. The corresponding LSVs for D-HOPG 60 min, D-HOPG 80 min, D-HOPG 100 min, and D-HOPG 120 min are shown in Fig. 3e. From the upper panel of Fig. 3f, it can be seen that the current densities of different N-HOPGs at the potential of 0.7 V vs RHE (the fastest kinetics

variation of ORR) only increase slightly from 0.09 to 0.13 mA/cm^2. Meanwhile, it is noted that the disorder level (the ratio of I_D/I_G) from Raman spectra for these four N-HOPGs keeps almost constant (Supplementary Fig. 4a). Thus, the influence of the N-dopant level on the ORR performance of N-HOPGs can be seen, though defects should also contribute to the ORR activity. To exclude the influence of N dopants, we prepared the four D-HOPG samples by removing the Pr-N from the above mentioned four N-HOPGs. The ratios of I_D/I_G of D-HOPG 60 min, D-HOPG 80 min, D-HOPG 100 min and D-HOPG 120 min are found to be 0.03, 0.05, 0.09 and 0.13, respectively (Supplementary Fig. 4b), which is directly correlated to the defect densities (Supplementary Fig. 5). Also, it is observed that the current densities are significantly increased with increasing the defect density in D-HOPGs (Fig. 3e). The current densities of different D-HOPGs at the potential of 0.7 V vs RHE are also found to be proportionally increased with increasing the defect density in D-HOPGs (the lower panel of Fig. 3f). The specific activities of the N-HOPG and D-HOPG are further evaluated by normalizing the catalytic performance to each active site (N-doping or defect site) (see Methods). Supplementary Fig. 6a shows much higher specific activities for D-HOPG 120 min with respect to N-HOPG 120 min below the onset potential (0.7 V), which is in line with the LSVs in Fig. 3b. Furthermore, it is found that the acidic ORR specific activity of the catalysts is decreased with increasing the concentration of active sites of Pr-N in N-HOPG, but increased with increasing the pentagon defect sites in D-HOPG (Supplementary Fig. 6b), suggesting that the pentagon defects are the major active sites for the enhanced acidic ORR[28]. The reduced specific activity per Pr-N with increasing the concentration of Pr-N may be attributed to deactivation of the Lewis basic site of C atom between two Pr-N sites on zigzag edge[29].

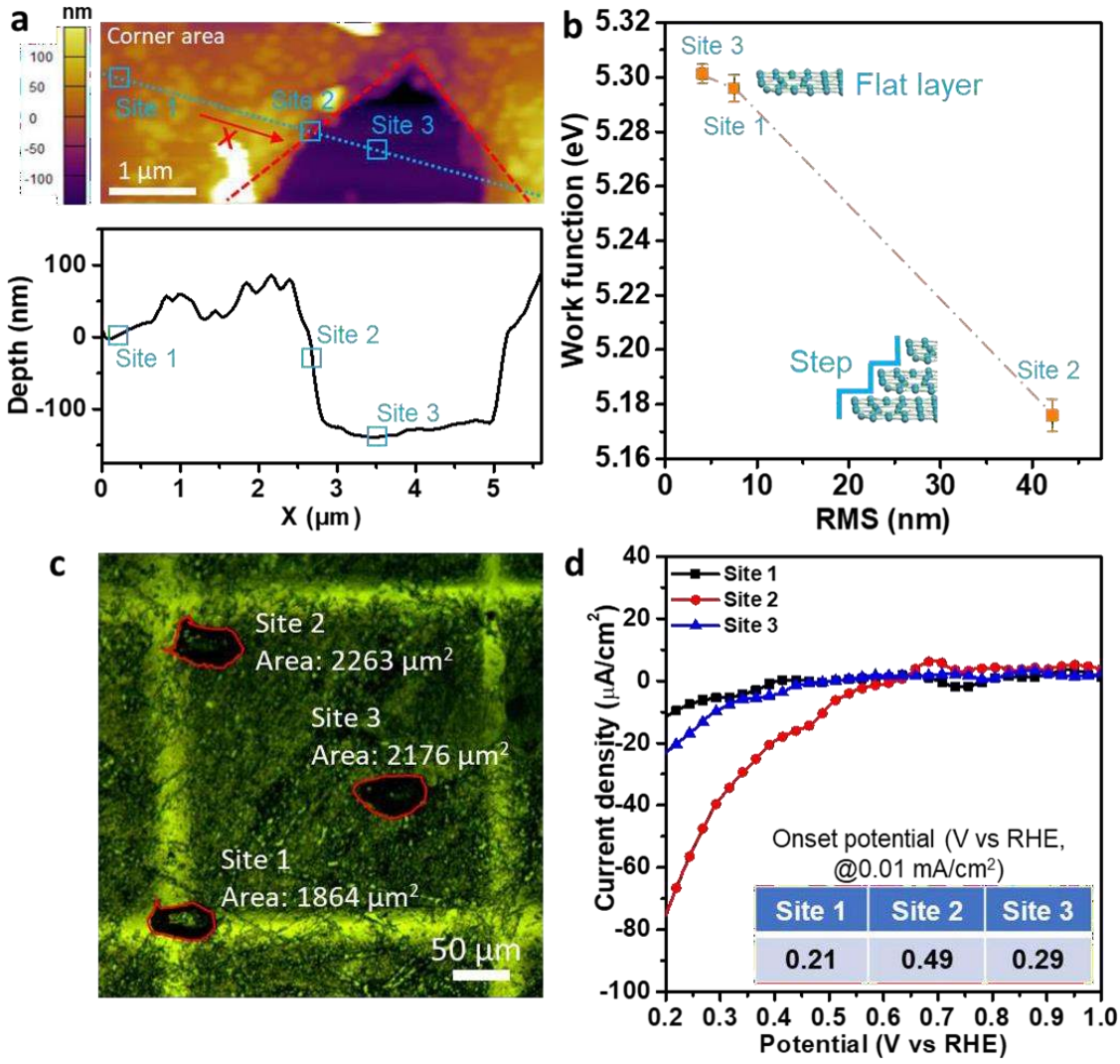

Fig. 4 | Identification of active location in D-HOPG via KPFM and micro-electrocatalytic analysis. a, The AFM line scan (along X axis marked on the image) of the depth in D-HOPG. **b,** Correlation of the local work functions and the roughness collected from three different regions on D-HOPG. The three corresponding areas are marked as site 1, site 2 and site 3 in (**a**). Error bars correspond to s.d. from three independent measurements. **c,** The optical microscope image of the D-HOPG (80 mesh). The electrolyte droplets are marked with red lines, denoted as site 1, site 2 and site 3

respectively. **d,** The LSV curves of site 1, site 2 and site 3 on D-HOPG (80 mesh) for ORR. The correlated onset potentials are shown in the inset table.

Identification of the active site location in D-HOPG. To further unveil the active sites in D-HOPG, we investigated the local work functions at different regions on D-HOPG. As shown in Fig. 4a, three typical sites (site 1, site 2 and site 3 corresponding to the top, edge and bottom of the groove structure, respectively) were selected for measuring the local work functions (Fig. 4a). Fig. 4b shows a similar local work function of ~5.30 eV for the site 1 and site 3, and an obviously lower value of ~5.17 eV for the site 2, implying that the edge areas of D-HOPG may have acted as the active sites for ORR. We further investigated the underlying relationship between the local work function and the count of the exposed edges (Fig. 4b), the latter is represented by the root mean squares (RMS) of the height deviations calculated from the surface roughness imagined by local surface scanning. As seen in Fig. 4b, the site 2 with the lowest local work function shows the highest RMS, indicating that the high catalytic activity of the site 2 is originated from the exposed edges.

In this study, we have also designed a micro-electrocatalytic testing apparatus to experimentally identify the active site location(s) in D-HOPG for ORR. As shown in Supplementary Fig. 7, micro-Pt counter electrode and Ag/AgCl reference electrode were encapsulated in a capillary tube while the D-HOPG (80 mesh) was used as the working electrode, on which three droplets sized approximately 50 μm were deposited at three different sites (denoted as: site 1, site 2 and site 3). As shown in Fig. 4c, the site 1 is dominantly on the top and site 2 stretches across the edge while site 3 is on the bottom of the patterned structure. Fig. 4d shows the LSV curves of site 1, site 2 and site 3 for ORR. As seen in Fig. 4d, the site 2 exhibits an onset potential of 0.49 V vs RHE, whilst the onset potentials of site 1 and site 3 are 0.21 and 0.29 V vs

RHE respectively, much more sluggish than that of site 2. These results clearly demonstrate that the ORR activity of D-HOPG is mainly arising from defects at the edge surface, but not the top and bottom regions.

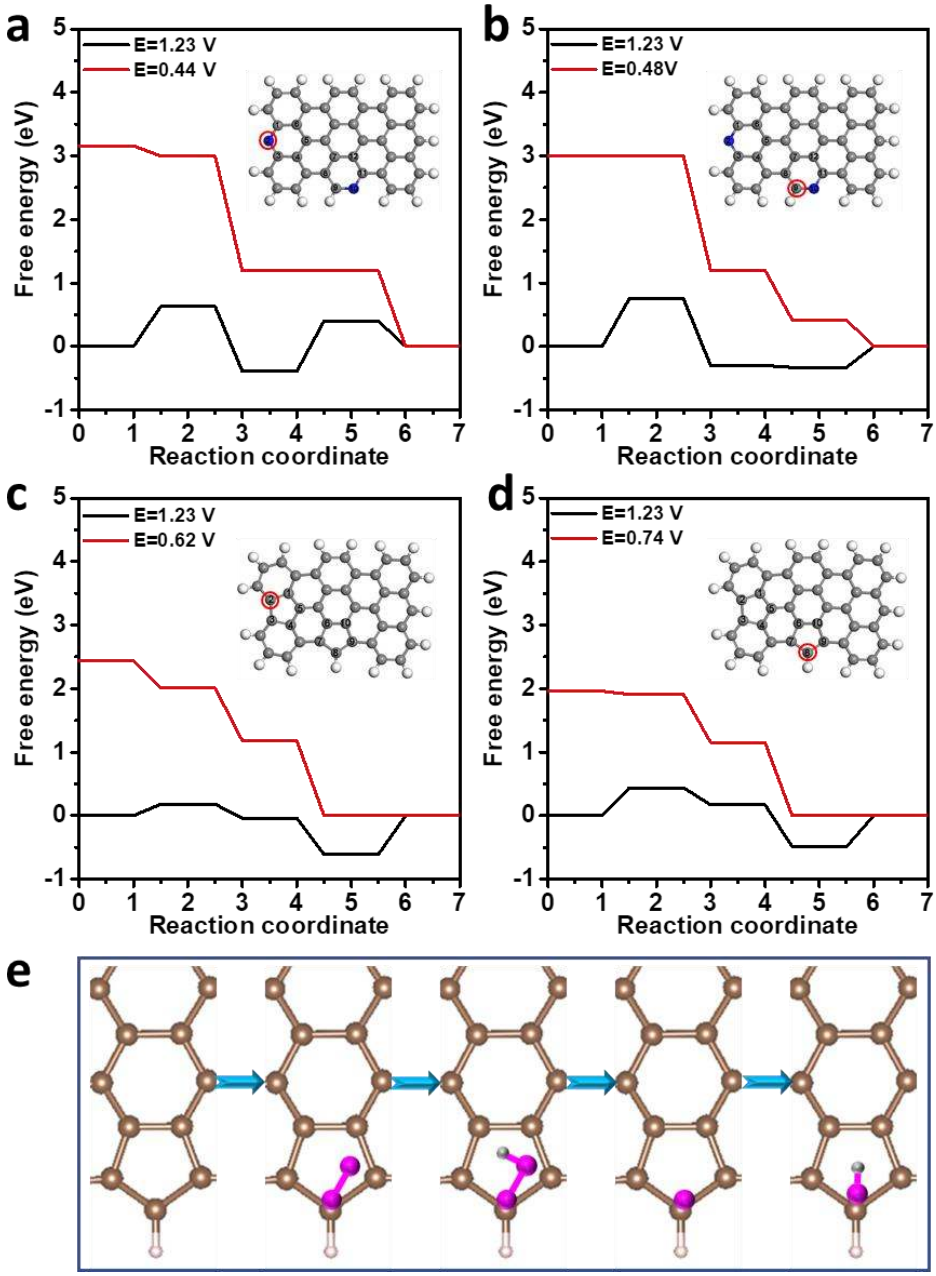

Fig. 5 | Unveiling the derived carbon defect as active site for enhanced ORR. a-d, The energy profiles of N2 (A), N9 (B), D2 (C) and D8 (D) for ORR. The topological structures are inserted. **e,** The ORR reaction pathway on D8 under acidic condition.

DFT calculations. Based on the above structural characterization, we performed density functional theory (DFT) calculations for the four carbon-based topological models (unit cell size of A=21.3 Å and B=12.3 Å; Vacuum=20 Å) shown in Supplementary Fig. 8a and b. The models contain two Pr-N atoms (Supplementary Fig. 8c) and two pentagons (Supplementary Fig. 8d) on the armchair and zigzag edges, respectively. The calculated energy profiles of different sites on the four models are given in Supplementary Fig. 9 and Supplementary Fig. 10. The most energetically favourable atoms on each model for ORR are illustrated in the Fig. 5a-d. It can be seen that D8 (Fig. 5d) is the preferential active site for ORR with the largest onset potential of 0.74 V. It is also noteworthy that the large uphill energy gaps in the first elementary reaction of N2 (Fig. 5a) and N9 (Fig. 5b) for ORR hamper the adsorption of reactant and increase the required overpotentials, leading to the observed higher ORR activity for defects than that of the N dopants. Fig. 5e shows the $4e^-$ ORR pathway on D8, which involves four protic hydrogen and electron transfer steps: (i) the adsorbed O_2 transfers into OOH*; (ii) desorption of H_2O and formation of O*; (iii) OH* is formed and (iv) the OH* further associates with a protic H and an electron to generate H_2O. Moreover, to investigate whether there is a synergistic effect between the pair of Pr-N or pentagon defects, the DFT calculations were performed using the models with only a single site (Pr-N or pentagon) in the position of zigzag Pr-N, armchair Pr-N, zigzag pentagon and armchair pentagon (Supplementary Fig. 11). The calculated overpotentials of N2', N9', D2' and D8' for ORR are 0.74, 0.7, 0.7 and 0.52 V, respectively, which are close to those of N2, N9, D2

and D8 in Fig. 5. This clearly indicates that the defect-defect interaction is very weak in the pair with a distance of one hexagonal ring thus its effect on the experimental result is limited.

Conclusions

In summary, we have demonstrated, through a combined theoretical and experimental approach, that the removal of Pr-N atom from an N-doped six-carbon ring in HOPG can form a pentagon defect at the edge. Importantly, macro/micro-electrochemical measurements, coupled with work function and DFT analyses, reveal that the edge pentagon defect thus produced as the major active site for acidic ORR, superior to that of Pr-N in N-doped HOPG. In this study, therefore, we have not only clarified a long-standing issue on the activity origin of carbon-based metal-free electrocatalysts for acidic ORR, but also provided a promising strategy for controlled synthesis of a specific type of carbon defects of high acidic ORR activities.

Methods

Synthesis of Ar-HOPG. The Ar-HOPG was fabricated from the commercial HOPG sheet (10 nm×10 nm) by plasma treatment through a nickel mesh under the atmosphere of Argon at 100 Watts. Then, the obtained sample was washed with nitric acid for three times to remove the residual nickel on the surface.

Synthesis of N-HOPG and D-HOPG. The Ar-HOPG was annealed at 700 °C for 3 hours in the ammonia flow. The prepared sample was denoted as N-HOPG. It was further annealed at 1150 °C for 2 hours under nitrogen to obtain D-HOPG.

Characterization. Raman spectrum was recorded on a Renishaw InVia spectrometer with a model 100 Ramascope optical fibre instrument. X-ray photoelectron spectrum (XPS) data were collected on a Kratos Axis ULTRA X-ray photoelectron spectrometer, and the binding energy of the C 1s

peak at 284.8 eV was used as an internal reference. Scanning transmission electron microscopy-Energy-dispersive X-ray spectroscopy (STEM-EDS) elemental mapping images were obtained from TECNAI G2 F20 with an acceleration voltage of 200 kV. High angle annular dark field (HAADF) images and BF images are collected from a probe-corrected JEOL ARM200F with an acceleration voltage of 80 kV.

Electrochemical measurements. All the electrochemical tests were performed in a conventional three-electrode system on an electrochemical station (CHI 760E), using Ag/AgCl (saturated KCl solution) electrode as the reference electrode and graphitic carbon rod as the counter electrode. All potentials were referred to the reversible hydrogen electrode (RHE) by following calculations: E (vs RHE) = E (vs Ag/AgCl) + 0.197 + 0.059pH. The micro-electrocatalytic measurements were conducted inside a deposited droplet of aqueous electrolyte, as previously reported [30].

The calculation of specific activity per active site. The specific activity is the performance normalized to single active site, calculated by:

$$\text{Specific activity} = \frac{N_{electrons}}{N_{active\ site}} \quad (1)$$

In this paper, the active site of N-HOPG and D-HOPG are recognized to be the Pr-N and pentagon, respectively. According to that the pentagon is generated from the removal of Pr-N, the number of pentagon is equal to the number of Pr-N. Thus the equation could be transformed to[16]:

$$\text{Specific activity} = \frac{j_{OR}(\frac{mA}{cm^2})\times 0.001(\frac{A}{mA})\times N_e per\ coulomb\ per\ second(\frac{e}{A\cdot s})}{D_{atom} in\ graphene\ (\frac{atoms}{cm^2})\times \rho_{PrN}(at\%)} = \frac{j_{OR}(\frac{mA}{cm^2})\times 0.001(\frac{A}{mA})\times 6.24\times 10^{18}(\frac{e}{A\cdot s})}{3.82\times 10^{15}(\frac{atoms}{cm^2})\times \rho_{PrN}(at\%)} \quad (2)$$

Calculation of root mean squares. The root mean squares (RMS) are the representations of surface roughness and calculated by:

$$RMS = [(1/L) \int_0^L (x)^2 \, dx]^{1/2} \quad (3)$$

Calculation of defect density. The defect density n_D is calculated by the following equation:

$$\frac{I_D}{I_G} = \frac{C(r^2 - r^2)}{(r_A^2 - 2r_S^2)}[e^{-\pi r_S n_D/10} - e^{-\pi (r_A - r)_D/10}] \quad (4)$$

The r_S is the average radii of defect area. Here, the size of pentagon defect is approximately 0.25 nm. The r_A is the radii of the area activated by the defect, which is 0.75 nm here. The factor C_A is determined by the excited laser and we used 4.2 here[31].

Density functional theory calculations. In this work, Density functional theory (DFT) calculations were carried out by using the Vienna *ab* Initio Simulation package (VASP)[32,33]. The ion–electron interactions were described by the projector augmented wave (PAW) approach. Electron exchange–correlations were represented by the functional of Perdew, Burke and Ernzerhof (PBE) of generalized gradient approximation (GGA)[34]. To ensure the convergence for total energy, all calculations were performed using a plane-wave cutoff energy of 400eV with Fermi-level smearing of 0.1 eV and Monkhorst-Pack grid (3×3×1) was used for k-point sampling. Besides, the convergence threshold of energy and forces were set to be 1×10^{-5} eV and 0.02 eV/Å, respectively.

The overall oxygen reduction reaction (ORR) in acidic environment can be written[35]:

$$O_2 + 4H^+ + 4e^- \rightarrow 2H_2O \quad (5)$$

And we divided ORR reaction into four steps:

1) $O_2 + H^+ + e^- + * \rightarrow OOH^*$ (6)

2) $OOH^* + H^+ + e^- \rightarrow O^* + H_2O$ (7)

3) $O^* + H^+ + e^- \rightarrow OH^*$ (8)

4) $OH^* + H^+ + e^- \rightarrow H_2O + *$ (9)

in which * implies the adsorption site.

For each step, the reaction free energy ΔG is defined by following equation[35]:

5) $\Delta = \Delta E + \Delta ZPE - T\Delta S + \Delta G_U + \Delta G_{pH}$ (10)

The ΔE, ΔZPE, and ΔS are the different energy, zero-point energy, and entropy of the reaction, respectively. The ΔE is calculated by DFT, ΔZPE and ΔS are obtained from the values of Table I in ref.[36].

Data availability

The data that support the plots within this paper and other findings of this study are available from the corresponding author upon reasonable request.

References

1 Gong, K. P., Du, F., Xia, Z. H., Durstock, M. & Dai, L. M. Nitrogen-Doped Carbon Nanotube Arrays with High Electrocatalytic Activity for Oxygen Reduction. *Science* **323**, 760-764 (2009).

2 Kurak, K. A. & Anderson, A. B. Nitrogen-Treated Graphite and Oxygen Electroreduction on Pyridinic Edge Sites. *J. Phys. Chem. C* **113**, 6730-6734 (2009).

3 Kundu, S. *et al.* Electrocatalytic Activity and Stability of Nitrogen-Containing Carbon Nanotubes in the Oxygen Reduction Reaction. *J. Phys. Chem. C* **113**, 14302-14310 (2009).

4 Geng, D. S. *et al.* High oxygen-reduction activity and durability of nitrogen-doped graphene. *Energy Environ. Sci.* **4**, 760-764 (2011).

5 Zhang, L. P. & Xia, Z. H. Mechanisms of Oxygen Reduction Reaction on Nitrogen-Doped Graphene for Fuel Cells. *J. Phys. Chem. C* **115**, 11170-11176 (2011).

6 Yasuda, S., Yu, L., Kim, J. & Murakoshi, K. Selective nitrogen doping in graphene for oxygen reduction reactions. *Chem. Commun.* **49**, 9627-9629 (2013).

7 Zheng, B., Wang, J., Wang, F. B. & Xia, X. H. Synthesis of nitrogen doped graphene with high electrocatalytic activity toward oxygen reduction reaction. *Electrochem. Commun.* **28**, 24-26 (2013).
8 Jiao, Y., Zheng, Y., Jaroniec, M. & Qiao, S. Z. Origin of the Electrocatalytic Oxygen Reduction Activity of Graphene-Based Catalysts: A Roadnnap to Achieve the Best Performance. *J. Am. Chem. Soc.* **136**, 4394-4403 (2014).
9 Wu, J. J. *et al.* Nitrogen-Doped Graphene with Pyridinic Dominance as a Highly Active and Stable Electrocatalyst for Oxygen Reduction. *ACS Appl. Mater. Interfaces* **7**, 14763-14769 (2015).
10 Liu, X. & Dai, L. M. Carbon-based metal-free catalysts. *Nat. Rev. Mater.* **1**, 16064 (2016).
11 Rao, C. V., Cabrera, C. R. & Ishikawa, Y. In Search of the Active Site in Nitrogen-Doped Carbon Nanotube Electrodes for the Oxygen Reduction Reaction. *J. Phys. Chem. Lett.* **1**, 2622-2627 (2010).
12 Lai, L. F. *et al.* Exploration of the active center structure of nitrogen-doped graphene-based catalysts for oxygen reduction reaction. *Energy Environ. Sci.* **5**, 7936-7942 (2012).
13 Niwa, H. *et al.* X-ray absorption analysis of nitrogen contribution to oxygen reduction reaction in carbon alloy cathode catalysts for polymer electrolyte fuel cells. *J. Power Sources* **187**, 93-97 (2009).
14 Liu, R. L., Wu, D. Q., Feng, X. L. & Mullen, K. Nitrogen-Doped Ordered Mesoporous Graphitic Arrays with High Electrocatalytic Activity for Oxygen Reduction. *Angew. Chem.-Int. Edit.* **49**, 2565-2569 (2010).
15 Lin, Z. Y., Waller, G. H., Liu, Y., Liu, M. L. & Wong, C. P. 3D Nitrogen-doped graphene prepared by pyrolysis of graphene oxide with polypyrrole for electrocatalysis of oxygen reduction reaction. *Nano Energy* **2**, 241-248 (2013).
16 Guo, D. H. *et al.* Active sites of nitrogen-doped carbon materials for oxygen reduction reaction clarified using model catalysts. *Science* **351**, 361-365 (2016).
17 Jia, Y., Chen, J. & Yao, X. D. Defect electrocatalytic mechanism: concept, topological structure and perspective. *Mat. Chem. Front.* **2**, 1250-1268 (2018).
18 Banhart, F., Kotakoski, J. & Krasheninnikov, A. V. Structural Defects in Graphene. *ACS Nano***5**, 26-41 (2011).
19 Hou, Z. F. *et al.* Electronic structure of N-doped graphene with native point defects. *Phys. Rev. B* **87**, 165401 (2013).
20 Tang, C. *et al.* Topological Defects in Metal-Free Nanocarbon for Oxygen Electrocatalysis. *Adv. Mater.* **28**, 6845-6851 (2016).
21 Tao, L. *et al.* Edge-rich and dopant-free graphene as a highly efficient metal-free electrocatalyst for the oxygen reduction reaction. *Chem. Commun.* **52**, 2764-2767 (2016).
22 Jiang, Y. F. *et al.* Significant Contribution of Intrinsic Carbon Defects to Oxygen Reduction Activity. *ACS Catal.* **5**, 6707-6712 (2015).
23 Jia, Y. *et al.* Defect Graphene as a Trifunctional Catalyst for Electrochemical Reactions. *Adv. Mater.* **28**, 9532-9538 (2016).
24 Rauf, M. *et al.* Insight into the different ORR catalytic activity of Fe/N/C between acidic and alkaline media: Protonation of pyridinic nitrogen. *Electrochem. Commun.* **73**, 71-74 (2016).
25 Yan, D. F. *et al.* Defect Chemistry of Nonprecious-Metal Electrocatalysts for Oxygen Reactions. *Adv. Mater.* **29**, 1606459 (2017).
26 Ji, L. W. *et al.* Graphene Oxide as a Sulfur Immobilizer in High Performance Lithium/Sulfur Cells. *J. Am. Chem. Soc.* **133**, 18522-18525 (2011).
27 Cheon, J. Y. *et al.* Intrinsic Relationship between Enhanced Oxygen Reduction Reaction Activity and Nanoscale Work Function of Doped Carbons. *J. Am. Chem. Soc.* **136**, 8875-8878 (2014).
28 Zhang, L. P., Xu, Q., Niu, J. B. & Xia, Z. H. Role of lattice defects in catalytic activities of graphene clusters for fuel cells. *Phys.Chem.Chem.Phys*. **17**, 16733-16743 (2015).

29 Hong, M., Chen, J. W., Chen & E. Y.-X, *Chem. Rev.* **118**, 10551−10616 (2018).
30 Shen, A. L. *et al.* Oxygen Reduction Reaction in a Droplet on Graphite: Direct Evidence that the Edge Is More Active than the Basal Plane. *Angew. Chem.-Int. Edit.* **53**, 10804-10808 (2014).
31 Lucchese, M. M. *et al.* Quantifying ion-induced defects and Raman relaxation length in graphene. *Carbon* **48**, 1592 – 1597 (2010).
32 Kresse, G. & Furthmuller, J. Efficiency of ab-initio total energy calculations for metals and semiconductors using a plane-wave basis set. *Comput. Mater. Sci.* **6**, 15-50 (1996).
33 Kresse, G. & Furthmuller, J. Efficient iterative schemes for ab initio total-energy calculations using a plane-wave basis set. *Phys. Rev. B* **54**, 11169-11186 (1996).
34 Perdew, J. P., Burke, K. & Ernzerhof, M. Generalized gradient approximation made simple. *Phys. Rev. Lett.* **77**, 3865-3868 (1996).
35 Li, D. *et al.* A Defect-Driven Metal-free Electrocatalyst for Oxygen Reduction in Acidic Electrolyte. *Chem* **4**, 2345-2356 (2018).
36 Valdes, A., Qu, Z. W., Kroes, G. J., Rossmeisl, J. & Norskov, J. K. Oxidation and photo-oxidation of water on TiO2 surface. *J. Phys. Chem. C* **112**, 9872-9879 (2008).

Acknowledgements

The authors thank the financial support from Australia Re-search Council (ARC DP170103317, DP170102267 and ARC DP190103881). Y.J. also thanks ARC Discovery Early Career Researcher Award (ARC DE180101030). The authors would like to thank the Australian National Fabrication Facility (ANFF) – Materials node, University of Wollongong (UOW) Electron Microscopy Centre (EMC) and Canadian Light Source for equipment access.

Author contributions

X.Y. and L.D. conceived and designed the project. X.Y. supervised the project. Y.J. and L.Zhang prepared the samples and did the electrocatalytic performances test. L.Zhang, L.Zhuang, X.Y. and Z.Z. performed the characterizations including XPS, SEM and Raman. J.W. did XAS. J.C. performed TEM. X.W., J.L. and Y.Z. performed PA. E.T. did AFM. Z.X. and S.W. performed micro-electrocatalytic measurement. H.L. and D.Y. performed the DFT calculations. Y.J., L.Zhang, X.Y. and L.D. wrote the manuscript. Y.J. and L.Zhang contributed equally to this work. All authors discussed the results and commented on the manuscript.

Competing interests

The authors declare no competing interests.